# HOKKAIDO UNIVERSITY

| | |
|---|---|
| Title | Filamentary switching of ReRAM investigated by in-situ TEM |
| Author(s) | Arita, Masashi; Tsurumaki-Fukuchi, Atsushi; Takahashi, Yasuo |
| Citation | Japanese Journal of Applied Physics (JJAP), 59, SG0803<br>https://doi.org/10.35848/1347-4065/ab709d |
| Issue Date | 2020-04-01 |
| Doc URL | http://hdl.handle.net/2115/80771 |
| Rights | ©2020 The Japan Society of Applied Physics |
| Type | article |
| File Information | [JJAP-S1101537_HU-Arita]_for HUSCAP.pdf |

Instructions for use

# Filamentary switching of ReRAM investigated by in-situ TEM

Masashi Arita*, Atsushi Tsurumaki-Fukuchi and Yasuo Takahashi

Graduate School of Information Science and Technology, Hokkaido University

Kita-14, Nishi-9, Kita-ku, Sapporo 060-0814, Japan

E-mail: arita@nano.ist.hokudai.ac.jp

## Abstract

The filament operation of resistive random-access memory (ReRAM) was studied via in-situ transmission electron microscopy (in-situ TEM), and the contribution of the conductive filament to the resistance switching was experimentally confirmed. In addition to the operation principles, the device degradation mechanism was studied through repeated write/erase operations. The importance of controlling Cu movement in the switching layer was confirmed for stable CBRAM (conductive bridge random access memory) operations. A device structure with double switching layers and device miniaturization was effective in restricting over accumulation of Cu in the switching layer and localizing the filament. This may improve the robustness of the device against performance degradation.

# 1. Introduction

Resistive random-access memory (ReRAM) provides high-speed operation, a wide memory window, and high-density storage. It is a candidate for use as memory in next-generation applications, such as storage-class memory that fills the storage gap between dynamic random access memory (DRAM) and flash memory [1-6]. In addition to the binary operation, its multi-level or analogue memory function and non-linear hysteretic current-to-voltage (*I-V*) properties have attracted significant attention for application as artificial synapses used in artificial neural network hardware [7-15]. Because of these promising potential applications, a large number of studies have investigated ReRAMs, ranging from materials and devices to circuits [16-33]. Their integration into practical memory chips has continued to advance and a 16 Gbit memory chip was reported with write and read speeds of 180 MB/s and 900 MB/s, respectively [34]. However, while the fundamental operating mechanism can be explained based on the electrochemical reaction [16-18], the cyclic resistance switching and device degradation mechanisms have not yet been fully understood. While there are some examples of commercialized ReRAM chips, a lack of knowledge of the switching mechanism limits its mass production and application [35].

A ReRAM device has a metal-insulator-metal (MIM) structure composed of a thin insulating switching layer (SL) sandwiched between a top electrode (TE) and a bottom electrode (BE) (Fig. 1a). The pristine device is normally in the high resistance state (HRS), and it converts into the low resistance state (LRS) by application of a voltage between the TE and BE. This is called the *Set* operation that is used for memory writing, and the first *Set* from the pristine state is called *Forming*. To prevent device failure caused by the abrupt current jump during the *Set* operation, the current is restricted (current compliance) using a field effect transistor (FET) (Fig. 1b) or by the electric source (Fig. 1c). It should be taken into consideration that the horizontal axis of the *I-V* switching curve usually corresponds with the output voltage from the electric source rather than the actual voltage applied to the ReRAM device (Figs. 1b-1c). Subsequent application of a voltage returns the resistance to the HRS, which is the *Reset* operation for memory erasure. The HRS/LRS resistance ratio is above 10 and it occasionally reaches up to $10^6$. The device operation can be classified into two categories: *unipolar* operation, where the *Set* and *Reset* operations can occur at the same polarity; and *bipolar* operation, where opposite voltage polarities are used for the *Set* and *Reset* operations. Another classification based on the switching region also exists. Switching operation where the resistance of the LRS ($R_{LRS}$) is proportional to the device size occurs, *e.g.*, in ReRAMs using perovskite-type complex oxides [16-18]. In this case, the electronic state change at the interface or metal-insulator transition is the origin of the resistance switching. However, in materials such as transition metal oxides, the resistance $R_{LRS}$ does not depend on the device size. For this operating group, the conductive filament (CF) formed in the insulator by voltage application is considered to contribute to the resistance change between the HRS and the LRS, and thus the memory operation [16-18]. In this report, the latter case (*i.e.,* the CF memory operation) was investigated using in-situ TEM.
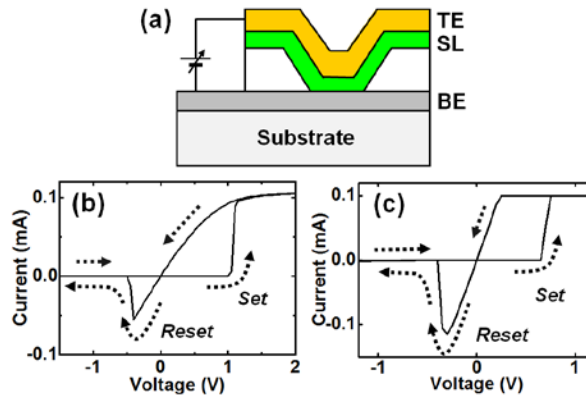
**Fig. 1** (a) Schematic cross-section of the ReRAM formed in the via hole of a thick insulator (white, *e.g.*, SiO$_2$ or SiN). The *I-V* switching curves with current compliance (b) by FET and (b) by an electric source.

*Unipolar* operation occurs because of the formation and rupture of the CF via a thermochemical reaction accompanied by dielectric breakdown. This type of ReRAM is called a TCM (thermochemical memory). *Bipolar* operation is considered to occur through an electrochemical redox reaction. When the TE or BE is made using electrochemically active metals such as Cu or Ag, the metal filament formed in the SL contributes to the memory operation. This type of ReRAM is called a conductive bridge RAM (CBRAM) or an electrochemical memory (ECM). In a *bipolar* ReRAM with electrodes made of non-active materials, such as Pt, the CF composed of oxygen vacancies is the basis of the memory operation. This is referred to as valence change memory (VCM) or OxRAM. While these discussions are analogous to dielectric breakdown and electroplating, they successfully explain the ReRAM operations. However, the information obtained from electric measurements are not satisfactory for understanding the switching parameters used for malfunction analyses, such as retention and endurance tests. In-situ transmission electron microscopy (in-situ TEM) measurements are complementary to electric measurements with cyclic switching operations, by which the microstructural evolution of the device can be observed simultaneously with the memory operation. In this manner, the formation/rupture of the CF can be directly observed and the origins of the device degradation can be visualized and analyzed.

The first studies on in-situ TEM of ReRAMs were reported around the year 2010 [35-39]. The formation and rupture of the CF on the *Set*/*Reset* operation of CBRAM was experimentally confirmed via in-situ TEM [41-43], and the CF formation process was categorized into four modes depending on the redox reaction rate and the mobility of the metal ions [44]. Over a number of in-situ TEM studies, the *Forming* and *Set* processes were clarified step by step [45-59]. However, the *Reset* process is still unclear and it is an important step for understanding the mechanism of device degradation. We have investigated the device microstructure of OxRAM and CBRAM influenced by switching operation. In this report, the role of the CF on ReRAM resistance switching and the microstructural evolution during device degradation studied via in-situ TEM are reviewed

with reference to our work carried out over the past decade.

## 2. Experimental

### 2.1 ReRAM film deposition

The ReRAM structure was in the form TE/SL/BE. Various deposition methods have been reported so far for ReRAM production: such as sputtering, atomic layer deposition (ALD), and pulsed laser deposition (PLD). For our work, radio frequency (RF) magnetron sputtering was used in an Ar or Ar+$O_2$ atmosphere. In certain cases, post-oxidation after film deposition was performed in air. For the TEM experiments, thin samples of less than 100 nm are required. In the following section, widely used sample processing techniques for in-situ TEM will be briefly explained.

### 2.2. Processing of in-situ TEM sample

The simplest method is the deposition of the SL on a wedge-shaped substrate that can function as the BE (Fig. 2a) [40, 60]. By attaching a nano-probe, which functions as the TE, to the SL the ReRAM is formed and operations can be carried out. By changing the probe position, multiple experiments can be done using one TEM sample. However, mechanical destruction can easily occur because of direct contact of the movable TE with the SL. In addition, long-term operations such as repeated switching are hard to carry out because of mechanical drift of the nano-probe. The ion-shadow method has been used to overcome these issues [61].

After dispersing carbon or diamond powders (black circles in Fig. 2c) on the ReRAM surface, $Ar^+$ ion milling is done. Because the milling rates for carbon and diamond are much lower than for the ReRAM materials, needle-shaped ReRAM nano-pillars with TE/SL/BE stacking can form (Figs.2c and 2d). Many ReRAM pillars can be obtained in one TEM sample, though there are disadvantages related to the positioning of the pillars, size dispersion, and the yield of the operation. One of the most popular method is the use of focused ion beam (FIB) processing. Multiple ReRAM devices with the same size can be processed on one TEM sample. While the position, size, and shape can be controlled as required, there is a possibility for the introduction of defects, such as electric shorting because of residual Ga from FIB processing and process damage at the surface and the interface. An example of a plain ReRAM chip subject after FIB processing is shown in Fig. 2e [49]. In Fig. 2f, nano-devices fabricated via lithography techniques were prepared by FIB for in-situ TEM [63]. Other innovative methods using FIB have also been reported for in-situ TEM of ReRAMs [64, 65]. In addition to the conventional vertical ReRAM structure (Fig. 1a), lateral ReRAM fabricated on a thin SiN membrane (Fig. 2g) have also been used in some reports [51, 67-70]. This was effective for high-resolution imaging because the sample thickness could easily be controlled to much less than 100 nm, and analysis at the nano- or atomic-level can be carried out.
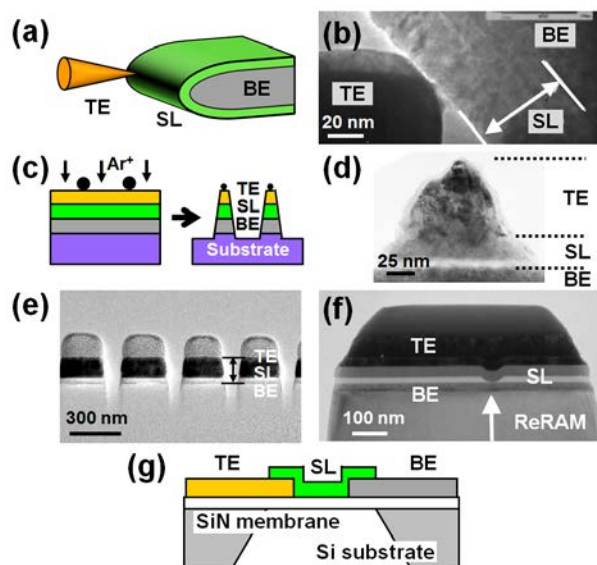
**Fig. 2** (a) Schematic of the wedge-shaped sample [49] and (b) an example of NiO-based OxRAM [60]. (c) Ion-shadow method to form ReRAM pillars (black circle: carbon or diamond powder) [49] and (d) an example of $MoO_x/Al_2O_3$-based CBRAM [62]. Examples of FIB processed in-situ TEM samples from (e) a stacked film ($MoO_x$-based CBRAM) [49] and (f) nanofabricated ReRAM cell (CuTe-based CBRAM) [63]. (g) Schematic of the lateral (or planar) CBRAM formed on a SiN membrane.

## 2.3. Experimental system and measurement

A schematic of the in-situ TEM experimental system is shown in Fig. 3a, where a home-made in-situ TEM holder with a piezo actuator (piezo holder) is attached to the electron microscope (Jeol JEM2010, 200 kV, $C_s$ = 0.5 mm). Selection of the device (or position) to be measured was accomplished using a Pt-Ir nano-probe, which can be moved via the piezo actuator placed in the piezo holder. As mentioned above, the device can easily be destroyed because of current overshoot on the *Set* operation. To prevent this, a kΩ load resistor is occasionally connected in series; however, even with this precaution, influence of current overshoot cannot be perfectly prevented because of the parasitic capacitance of the wiring in the TEM holder (~10 nF in our case). For example, a current overshoot in the mA range is expected when the resistance of the HRS ($R_{HRS}$) is converted to the LRS ($R_{LRS}$) of 10 kΩ within nanoseconds under the application of a 1 V bias. To restrict this current overshoot more effectively, a TEM holder with an FET was developed (Fig. 3b).

The switching operation was carried out using a source measure unit (SMU, Yokogawa GS820), and the dynamic change of the device microstructure was recorded as a video. The current was measured via the substrate in most cases. As described just above, the compliance current ($I_{comp}$) to restrict device destruction was controlled by using this SMU as well as the FET. The TEM electron beam did not have a marked influence on the microstructure, even when high-resolution measurements were carried out (~170 fA/nm$^2$ with an acceleration voltage of 200 kV). In the present in-situ TEM experiments, the TEM magnification was reduced to ~$10^4$–$10^5$, and the electron beam density was much lower than this value. The offset current contributed by the TEM electron

beam was less than the nA order and can be neglected because it was much smaller than the ReRAM operation current (several to hundreds of μA). The video contrast was occasionally enhanced and frame averaging was done to reduce the noise.
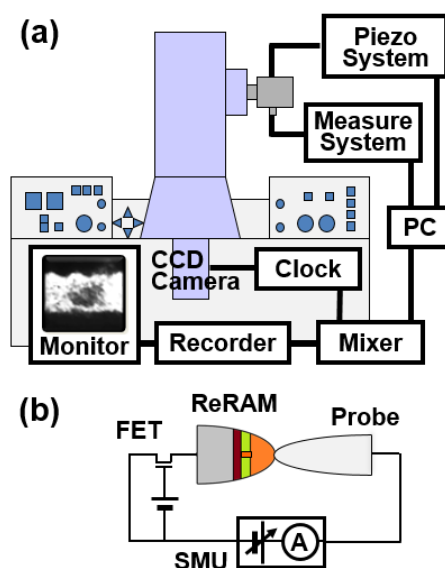


**Fig. 3**    (a) In-situ TEM system and (b) a schematic of the measurement circuit [49].

## 3. In-situ TEM of OxRAM

Many oxide films sandwiched between two non-active electrodes (*e.g.,* Pt and TiN) operate as TCM-type or VCM-type ReRAMs [17-19]. In-situ TEM studies reported to date have mainly studied the switching operation after *Forming*, and investigation of the *Forming* step itself is rare [39, 47]. Here, the *Forming* process of polycrystalline NiO is demonstrated [57, 71].

For this, the sample was fabricated via RF sputtering of Ni on a PtIr wedge followed by thermal oxidation to NiO in air. The pristine sample is shown in Fig. 2b, and the *Forming* results are shown in Fig. 4, where a load resistor of 10 kΩ was connected in series outside the TEM holder. *Forming* occurred at +1.7 V and the resistance decreased significantly (Fig. 4a). The resistance was almost equal to that of the load resistor and, hence, the ReRAM should have a smaller resistance than this value. Corresponding to this switching to the LRS, a bridge with a width of 40 nm formed (Fig. 4b). Using a nano-probe, it was confirmed that this bridge was in the LRS and the surrounding region was insulating. This bridge was the CF that contributed to the ReRAM operation. In addition, nano-regions of the NiO film were measured using this system, and it was clarified that the resistance at the grain boundaries was less than 1% of the bulk of the grains. As indicated in some reports [16], the CF seemed to be formed at the grain boundary. In Fig. 4c, the CF size is summarized as a function of the injected power [71, 72]. By reducing the switching power to $10^{-7}$ W, the formation of a CF of less than 10 nm is expected. The composition of the CF was measured via energy dispersive X-ray spectroscopy (EDS), and it was determined to be Ni:O = 85:15, while the surrounding region had an Ni:O composition ratio of 71:29. This fits to the general consensus that

the CF of the OxRAM is formed by oxygen vacancies.

However, the *Reset* operation for memory erasure could not be carried out because the device was destroyed during the process. This phenomenon is not unique to our investigation, and in-situ TEM reports on the *Reset* operation of TCM and VCM was quite rare [47]. The oxygen that drifted during the *Forming* and *Set* operations is considered to be captured in other regions of the device and used for rupture of the CF at *Reset* [18]. However, during in-situ TEM operation, which is performed in a vacuum, the oxygen escapes into the TEM vacuum atmosphere and is not present when required for the *Reset* [71]. For further understanding of the operation schemes of the TCM and VCM, a special in-situ TEM technique needs to be developed, for example, a method combining in-situ TEM and environmental TEM.
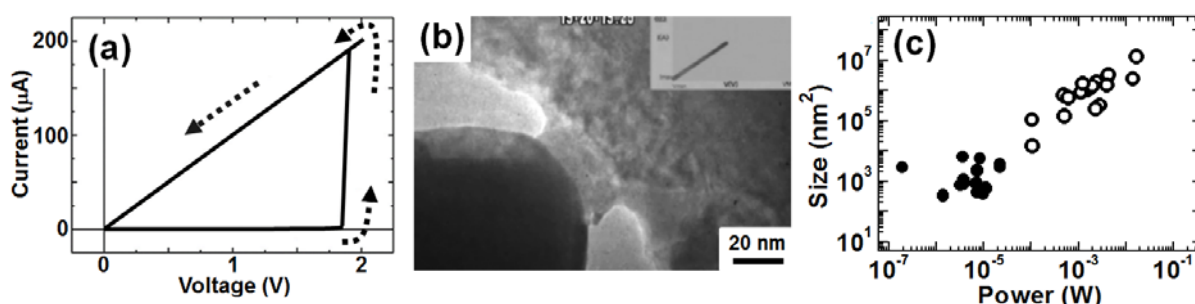


**Fig. 4** *Forming* of PtIr/NiO/PrIr OxRAM. (a) The *I-V* switching curve where the broken arrows indicate the direction of the voltage sweep. (b) In-situ TEM image after *Forming*. (c) The CF size vs. injected power. The black circles are data from in-situ TEM experiments while the white circles are the data observed in ReRAM devices with Pt electrodes measured outside the TEM [71, 72].

## 4. In-situ TEM of CBRAM

*4.1 Formation and erasure of the conductive filament corresponding to Set/Reset operation*

CBRAM is a type of ReRAM in which a metal CF is responsible for memory operations. Here, an example using Cu:GeS deposited on a PtIr wedge substrate will be discussed [41, 73]. The movable probe was grounded and served as the BE while the wedge substrate was biased and used as the TE. In this case, both the TE and the BE are made of PtIr, and the SL serves as the Cu source. The results are shown in Fig. 5. Figure 5a shows the *I-V* switching curve, which demonstrates a clear hysteretic curve of CBRAM. The corresponding TEM images are shown in Figs. 5b-5e. A CF with a dark contrast formed/vanished on application of the *Set*/*Reset* operation. From analyses of the in-situ TEM images, in-situ diffraction patterns, and in-situ EDS spectra, the following was summarized: by the positive voltage applied to the TE (substrate), Cu ions in the SL drifted to the cathode (BE: probe) and formed a Cu deposit at the surface of the cathode via the electrochemical redox reaction; they then grew towards the anode (TE: substrate) forming a CF, and the resistance was then set to the LRS. This fits with the electrochemical CF model that is widely accepted [16]. In contrast with these results, for example in CBRAM formed by $Ag/ZrO_2/Pt$, the CF grew from the

anode (Ag) to the cathode (Pt) [42]. A previous study discussed the filament growth using several metals, with four growth modes related to the redox rate of the metal and the mobility of metal ions in the electric field [44]. Based on that work, it is expected that the Cu ion mobility is high in GeS. In addition, the SL of our sample already contained Cu in the pristine state; therefore, the distance required for the Cu ions to reach the BE interface should be small. This may also contribute the CF growth from the BE (cathode).
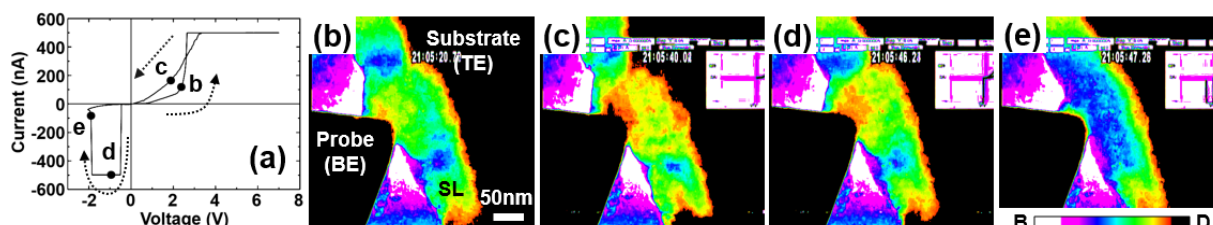


**Fig. 5**    In-situ TEM result of PtIr/Cu:GeS/PtIr CBRAM [41, 73]. (a) The *I-V* switching curve and (b-e) corresponding TEM images extracted from the recorded video. Pseudo color treatment was performed for clear identification of the CF. The meaning of the color is indicated in (e), white corresponds to bright contrast (B) and black to dark contrast (D).

By reversing the voltage polarity, the CF contracted from the BE (anode), and the resistance of the device changed to the HRS. However, the SL was different from the pristine state, which is demonstrated in Fig. 6. The CF in the 1st switching cycle is shown in Fig. 6a. Changing the probe position from A to B results in another cycle being carried out. The formed CF connected the probe and position A, but did not connect to the nearest position B (Fig. 6b). Once the CF formed, residual like Cu clusters may remain even after erasure. This was the origin of the phenomenon seen in Fig. 6. In general, the *Set* voltage is smaller than the *Forming* voltage, which can be explained by the contribution of the residuals.
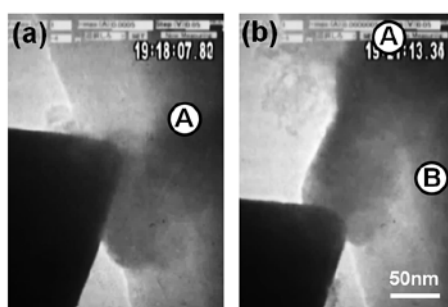


**Fig. 6**    Filament formation in (a) the 1st and (b) the 2nd *Set* with position change of the probe (BE) [73]. The positions A in (a) and (b) correspond with each other. The CF grew towards position A, where the first CF was formed, instead of position B, which is nearest to the probe.

*4.2 Switching repetition and formation/erasure of CF*

In this section, an example of the repeated *Set/Reset* switching is shown [46, 74-76]. The sample used was $Pt_{(100)}/Cu_{(30)}/MoO_{x(50)}$ formed on a TiN/Si substrate, and the number in parentheses is the thickness in nm. The sample was processed via the ion-shadow method, and its width was ~300 nm.

After several *I-V* sweeps to reduce the resistance without switching, clear CBRAM switching began. The device was operated using the voltage sweep mode (0.8 V/s) with a relatively higher current of more than 100 μA to observe the CF clearly. In the 1st switching cycle (Fig. 6a), an abrupt current increase occurred after state A, which was the *Set* operation. In the TEM image, a dark contrast region appeared from the Cu TE to the $MoO_x$ layer (state B). With further current flow after the *Set* (*over-Set*), the shape of this dark region changed and grew to form a Cu filament bridging the Cu and TiN electrodes (state C), and the LRS was achieved. Details can be seen in the the Suppl. Movie of ref. [76] (http://www.rsc.org/suppdata/c6/nr/c6nr02602h/c6nr02602h2.wmv). The time to reach the compliance current after the state A was 0.8 s, and the charge contributing the current flow is estimated as ~$6x10^{-5}$ C using the *I-V* curve. Assuming that the current was only the ionic current of $Cu^+$ or $Cu^{2+}$, the CF should be much larger than μm. This does not fit to Fig. 7. The total current should be contributed also by other factors like oxygen vacancies and electrons. With polarity reversal, the resistance increased significantly between states D and E (*Reset*), but no clear change could be observed in the TEM image. Rupturing of the filament in local region might contribute to this *Reset* operation though we could not success to detect it. With continued current flow (*over-Reset*), the current became unstable and the CF vanished from the BE side (HRS). In the 2nd cycle, the *Set* voltage became slightly lower (Fig. 6b), which is due to residual Cu in the $MoO_x$ layer. The CF grew from the BE to the TE. No clear change was observed in the CF contrast on the moment of the *Set* operation, it then grew to a 35 nm wide CF during the *over-Set*. The CF also did not show a clear change for the *Reset* process, and it vanished from the BE on the *over-Reset*. For the 3rd cycle, the CF grew from the BE as in the 2nd cycle (Fig. 6c). In this cycle, a pit formed at the TE interface during the CF growth, and thus the connection between the TE and CF appeared imperfect. While *Reset* switching was observed at -1.5 V, the CF did not show a change in morphology. It contracted from the CF surface during the *over-Reset*, and it disappeared towards the BE. In all cases, the current flow was an important factor for inducing a large change of the CF morphology.
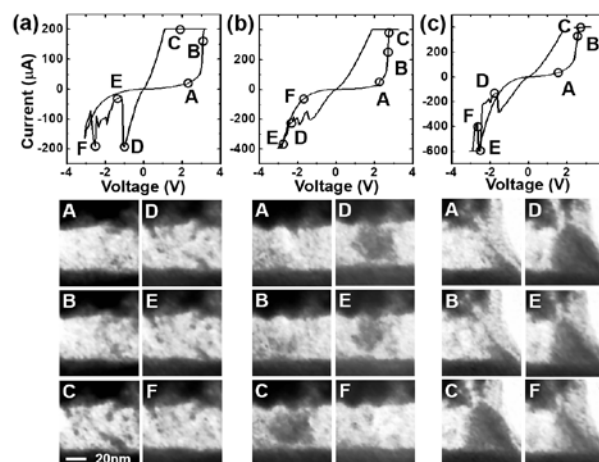


**Fig. 7** Filament formation and erasure observed in a series of switching cycles with increasing $I_{comp}$: (a) the 1st, (b) the 2nd and (c) the 3rd cycles. Sample is a $Cu/MoO_x/TiN$ stacking CBRAM. Alphabetic marks in the *I-V* curve and TEM photographs correspond each other [76].

From these results, it can be concluded that there are two *Set* modes and two *Reset* modes in the MoO$_x$ CBRAM (Fig. 8) [76]. With less Cu inclusion in the switching layer, as in the 1st cycle in Fig. 7a, Cu deposits appear from Cu in a manner similar to Ag/ZrO$_2$/Pt with low ion mobility [42]. They grew into the CF bridging two electrodes with consequent current flow (*Set-1*). In contrast, the Cu deposits appear at the BE interface when more Cu is included in the switching layer (such as the 2nd cycle or beyond: Figs. 7b and 7c). This occurs because of the short distance required for Cu ions to reach the BE. The Cu deposits are due to chemical reduction at the BE interface and it grows towards the TE (*Set-2*). The bridging between two electrodes occurs during the *over-Set*. In relation to the *Reset* operation, the CF contracted towards the BE when bridging was not satisfactory (*Reset-1*). The Cu is considered to dissolve from the CF surface into the SL with the help of the Joule heat caused by current flow, and the Cu ions move to the TE along the electric field. In contrast, the direction is the reverse when the bridging is satisfactory (*Reset-2*). This may be due to surface oxidation (ox-TiN) of the TiN BE. Because the resistance of this region must be high and Joule heat is mainly generated there, the dissolution of Cu is accelerated near the ox-TiN. In addition to the redox rate of Cu (or Ag) and the mobility of the ions [44], the inclusion of Cu (or Ag) is an important factor that influences the CF growth/erasure. This depends on the operation history of the CBRAM, and its control is important for extended switching cycles.
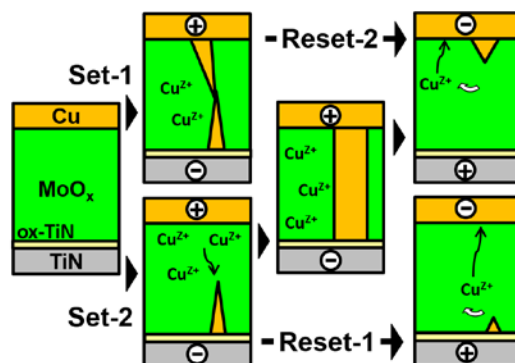


**Fig. 8**    Schematic of the *Set* and *Reset* operations [76]. There are two *Set* modes and two *Reset* modes depending on the switching history.
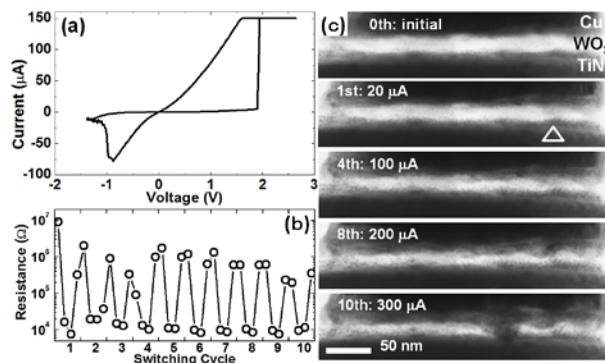
### 4.3 Device degradation

In this subsection, device degradation will be discussed using in-situ TEM data. In Fig. 9a, the whole device cross-section of the sample used in Fig. 7 can be seen [74]. By increasing the *Set* current ($I_{comp}$) from the 1st (200 µA), to the 2nd (400 µA), 3rd (400 µA) and 4th (600 µA) cycle, the CF grew significantly (Fig. 9b). A retention time that was longer than 5 min could be confirmed. This result indicated that the current enhances the CF growth. Another important observation from these TEM images is the CF position. One avenue to realize a large resistance ratio ($R_{HRS}/R_{LRS}$) is by achieving a large $R_{HRS}$ after a strong *Reset* (i.e., *over-Reset*). To understand the phenomenon occurring under these conditions, the CF was erased almost completely by an *over-Reset* in Fig. 9. The new CF appeared cycle by cycle and the CF position was significantly changed. A strong

erasure via the *over-Reset* may induce unstable operation because of removal of Cu residuals.
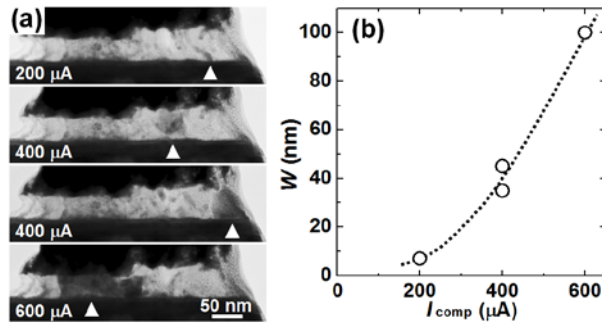


**Fig. 9**     Enlargement and position instability of the CF [74]. (a) TEM photographs after *Set* and (b) measured CF width (W) in relation to $I_{comp}$. The sample is a Cu/MoO$_x$/TiN stacked CBRAM.

Therefore, for the next experiment, repetitive operations were carried out without the *over-Reset* (Fig. 10). A Pt$_{(100)}$/Cu$_{(30)}$/WOx$_{(20)}$/TiN sample processed via the ion-shadow method was used and clear CBRAM operation was confirmed (Fig. 10a). The $I_{comp}$ for the *Set* operation was gradually increased, and it served a kind of acceleration test [77]. The resistance ratio of $R_{HRS}/R_{LRS}$ was ~100, and the $R_{HRS}$ decreased with increasing number of switching cycles, which can lead to HRS endurance failure. After much extended cycling, the device would no longer be able to realize resistance switching. In the TEM images during opearations, it can be seen that Cu moved into the WO$_x$ and formed layers at the interfaces in a wide area not only around the CF; as a result, the SL became thin. This indicated that current leakage aside from the CF induced Cu movement from the TE in the wide area, which is the origin of the HRS endurance failure. Reports have indicated that the device can be recovered after HRS endurance failure recovered by a strong *Reset* [78]. However, considering the results shown in Fig. 9, position instability of the CF occurs after a strong *Reset*. The power balance between the *Set* and *Reset* is important to control Cu movement and thus stable CBRAM memory operation.



**Fig. 10**     Device seen in a Cu/WOx/TiN stacked CBRAM [77]. (a) Typical *I-V* switching curve (6$^{th}$ cycle). (b) The endurance graph with increasing $I_{comp}$. A symptom of HRS degradation is seen. (c) Corresponding TEM images where the numbers in each figure denote the cycle number and $I_{comp}$. The triangle indicates the CF appeared in the 1$^{st}$ cycle. Deposition of Cu showing dark contrast is identified.

## 4.4 Double-layer CBRAM

The dispersion of Cu in a wide region of the SL causes device degradation as described above. Using the double SL structure is one available method to restrict device failure. Many reports have studied the double-layer ReRAM, and an improvement of memory performance has been reported [79-83]. In this subsection, the in-situ TEM study of a double SL CBRAM is presented. The used sample structure was $Cu_{(30)}/MoO_{x(20)}/Al_2O_{3(5)}$ formed on a TiN/Si substrate and was processed via the FIB technique [84-86]. The number in the parentheses indicates the film thickness in nm. A typical *Set* curve is shown in Fig. 11. In state-A at the start of the operation, clear stacking of the double-layer structure can be identified. After the *Set* switching began (state-B), the red colored region appeared around the interface between $MoO_x$ and $Al_2O_3$, which corresponds to the darkened region from the TEM image of state-A because of Cu accumulation. This grew into the $Al_2O_3$ layer when the current reached the compliance value (state-C). At the same time, a hole formed in the lower part of the Cu TE, which is shown with blue color. Copper from the TE drifted through the $MoO_x$ layer, and its movement was restricted at the $MoO_x/Al_2O_3$ interface and a deposit was formed there. Copper moved into the $Al_2O_3$ layer during subsequent current flow, and a CF appeared with detectable contrast. From this result, the Cu mobility in $Al_2O_3$ can be considered to be smaller than in $MoO_x$. By combination of the two insulator layers with different properties, the Cu movement can be restricted and the CF can be localized. Good switching properties of the double layer CBRAM, such as a high switching speed and stable operation with lower degradation, can be achieved by this limitation of CF growth.
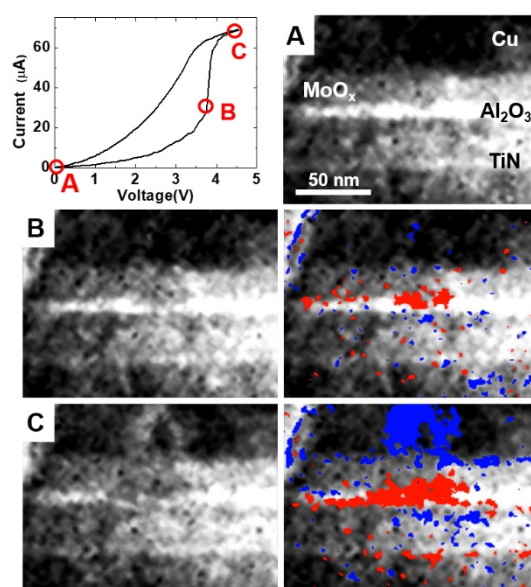


**Fig. 11**    Filament formation in the $Cu/MoO_x/Al_2O_3/TiN$ CBRAM with double switching layers. The *Set* switching curve and corresponding TEM images are shown. For states B and C, the original images (left column) and painted images (right column) are compared. In the region with red color, the image contrast became dark from the state-A, which indicates Cu accumulation. On the other hand, the contrast became bright in the blue region, and thus Cu moved out from this region. Note the linear arrangement of red and blue at the interface is the artefact caused by image drift during the observation.

## 4.5 Nanofabricated CBRAM device

Miniaturization of the CBRAM is a key factor for practical application. In this subsection, the application of in-situ TEM on CuTe-based nanofabricated CBRAM devices (30 or 70 nm in size) processed by FIB of the in-situ TEM sample (Fig. 2f) will be discussed [46, 63]. To investigate the performance, the *I-V* switching characteristics were tested for 60 cycles and the device achieved CBRAM operation without degradation. Next, the device was investigated by varying the $I_{comp}$. In Fig. 12, the TEM images before and after the *Set* and after the *Reset* are compared with the *I-V* switching curve. In all cases, clear switching curves were realized. However, the change in the image was very faint and was identified only when the $I_{comp}$ was large, as marked with a triangle in the image after a *Set* operation with $I_{comp}$ = 125 µA, which formed a CF in the nm scale. Therefore, the CF for 100 and 60 µA should be much smaller, and there was no detectable image contrast in this sample with a TEM sample thickness of ~100 nm. This was the same as the trend observed in Fig. 7: where a small current results in a small CF. To identify the composition of the CF, EDS mapping was carried out. As seen in Fig. 13, copper drifted into the SL while tellurium did not show such a trend. Hence, the CF identified in Fig. 12 was made up of Cu as other CBRAMs. The Cu filament appeared near the edge of the via hole, and concentration of the electric field seems to enhance the CF formation.
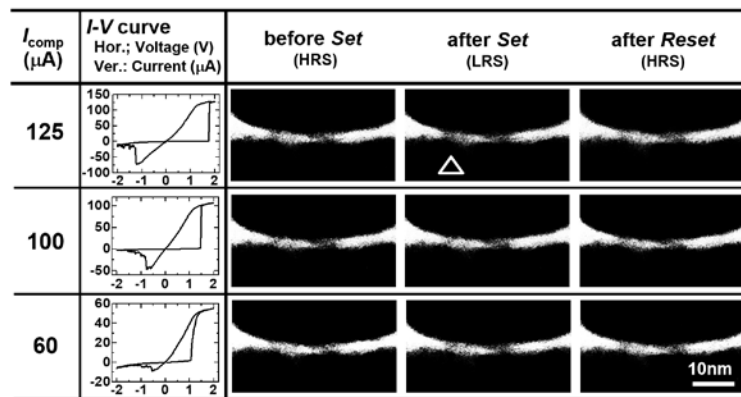


**Fig. 12**    The CF evolution observed in a CuTe-based nanofabricated CBRAM [63]. The margin of the switching region was enlarged and the contrast was significantly enhanced. The CF was identified only when a large current was passed in the operation (triangle), while clear memory operation was realized in all cases. Other filamentary contrast showed no change and did not contribute the switching operation.
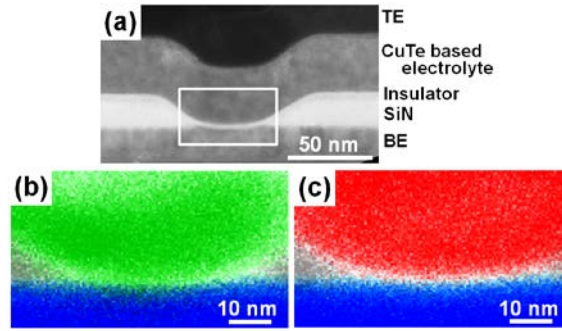
**Fig. 13** Composition analysis of the switching region after the *Set* operation, where a large current ($I_{comp}$ = 350 μA) was used to induce a large change [63]. (a) A conventional TEM image. The region in the square was analyzed. The EDS map for (b) Cu (green) and (c) Te (red) signals. The BE and the insulator are blue and white, respectively.

Though the CF was quite small, its retention property was good. Even when the CF was not detected in the TEM images, the LRS data were maintained for at least 3 months at room temperature when the $I_{comp}$ was > 40 μA (Fig. 14a). In addition, pulse switching repetition up to $10^5$ was confirmed inside the TEM microscope (Fig. 14b). Device miniaturization was important not only for integration but also for low-power operation through localization of the nano-sized CF, good memory retention, and good endurance property.
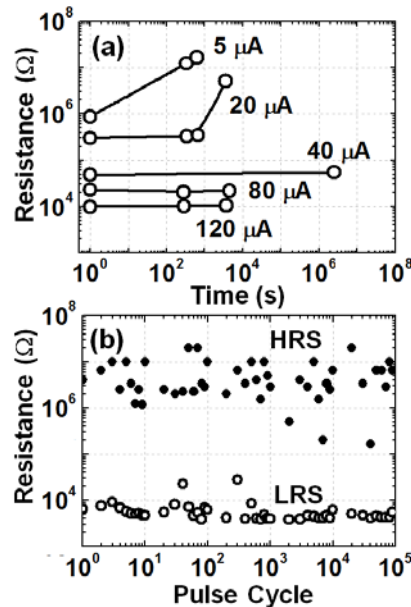


**Fig. 14** Degradation tests performed in a TEM microscope [63]. (a) Retention graph for various currents, and (b) endurance graph using the voltage pulses (+3.0 V/500 μs for *Set* and -1.5 V/100 μs for *Reset*).

## 5. Summary and Conclusion

In this contribution, we reviewed our in-situ TEM works on OxRAM and CBRAM. In both cases, filamentary switching was experimentally confirmed. Especially for Cu-based CBRAMS, repeated switching was realized, and switching details including device degradation could be discussed. The CF appeared/vanished on carrying out the *Set*/*Reset* operations. The CF size increased with the *Set* current; however, a remarkable change of the CF did not necessarily occur at

the moment of *Set/Reset* switching; a large change appeared with the subsequent current flow. The current was a key factor for controlling the CBRAM performance, and the power balance between *Set* and *Reset* operations is important. Cu deposits formed widely at the interface region when a strong *Reset* operation was not used, and the effective thickness of the switching layer was reduced, which leads to HRS endurance failure. While a strong *Reset* may prevent this degradation, the CF position changed during this process, which may cause switching instability. The operation robustness could be improved by using double switching layers. In this case, Cu movement during voltage application was restricted at the interface between two switching layers. This prevents the over-accumulation of Cu and stable switching can be expected. Localization of the CF is important and this was realized by adopting miniaturized CBRAM cells. A thin filament in the nm range was localized in a thin insulator layer, and a sharp and stable switching was realized at a low current.

As demonstrated in this report, in-situ TEM investigation has contributed significantly to understanding filamentary ReRAM operation. While the filaments shown in this report were mainly in the 10 nm size range, using tiny filaments may be important for stable switching repetition. For further understanding of the filamentary ReRAM operation, in-situ TEM at nanometer or atomic scale will be necessary.

**Acknowledgements**

**References**

[1]　International Technology Roadmap for Semiconductors, 2011 Edition, Emerging Research Devices (2011).

[2]　H. Akinaga: Japn. J. Appl. Phys. **52**, 100001 (2013).

[3]　D. Sacchetto, P.-E. Gaillardon, M. Zervas, S. Carrara, G. de Micheli, and Y. Leblebici: IEEE Circuits Syst. Mag. **13**, 23 (2013).

[4]　Y. Fujisaki: Japn. J. Appl. Phys. **52**, 040001 (2013).

[5]　K. Takeuchi: Japn. J. Appl. Phys. **55**, 04EA02 (2016)

[6]　J. Boukhobza, S. Rubini, R. Chen, and Z. Shao: ACM Trans. Des. Auto. Electr. Sys. **23**, 14 (2017).

[7] J. J. Yang, D. B. Strukov, and D. R. Stewart: Nat. Nanotech. **8**, 13 (2012).

[8] B. Gao, J. Kang, Z. Zhou, Z. Chen, P. Huang, L. Liu, and X. Liu: Japn. J. Appl. Phys. **55**, 04EA06 (2016).

[9] G. W. Burr, R. M. Shelby, A. Sebastian, S. Kim, S. Kim, S. Sidler, K. Virwani, M. Ishii, P. Narayanan, A. Fumarola, L. L. Sanches, I. Boybat, M. Le Gallo, K Moon, J. Woo, H. Hwang, and Y. Leblebici: Adv. Phys. X **2**, 89 (2017).

[10] S. H. Tan, P. Lin, H. Yeon, S. Choi, Y. Park, and J. Kim: APL Mater. **6**, 120901 (2018).

[11] D. Ielmini: Microelec. Eng. **190**, 44 (2018).

[12] R. Waser, R. Dittmann, S. Menzel, and T. Noll: Faraday Disc. **213**, 11 (2019).

[13] S. H. Jo, T. Chang, I. Ebong, B. B. Bhadviya, P. Mazumder, and W. Lu: Nano Lett. **10**, 1297 (2010).

[14] M. Prezioso, F. Merrikh-Bayat, B. D. Hoskins, G. C. Adam, K. K. Likharev, and D. B. Strukov: Nature **521**, 61 (2015).

[15] S. Park, M. Chu, J. Kim, J. Noh, M. Jeon, B. H. Lee, H. Hwang, B. Lee, and B. Lee: Sci. Repts. **5**, 102123 (2015).

[16] R. Waser, and M. Aono, Nat. Mater. **6**, 833 (2007).

[17] A. Sawa, Mater. Today **11**, 28 (2008).

[18] H. Akinaga, and H. Shima, Proc. IEEE **98**, 2237 (2010).

[19] T. Hasegawa, K. Terabe, T. Tsuruoka, and M. Aono: Adv. Mater. **24**, 252 (2012).

[20] S. Q. Liu, N. J. Wu, and A. Ignatiev: Appl. Phys. Lett. **76**, 2749 (2000).

[21] M. N. Kozicki, M. Park, and M. Mitkova: IEEE Trans. Nanotech. **4**, 331 (2005).

[22] S. Seo, M. J. Lee, D. H. Seo, E. J. Jeoung, D.-S. Suh, Y. S. Joung, I. K. Yoo, I. R. Hwang, S. H. Kim, I. S. Byun, J.-S. Kim, J. S. Choi, and B. H. Parka: Appl. Phys. Lett. **85**, 5655 (2004).

[23] K. Aratani, K. Ohba, T. Mizuguchi, S. Yasuda, T. Shiimoto, T. Tsushima, T. Sone, K. Endo, A. Kouchiyama, S. Sasaki, A. Maesaka, N. Yamada, and H. Narisawa: Tech. Dig. Internat. Electr. Dev. Meet. (IEDM) (2007) pp. 783.

[24] Z.Wei, Y. Kanzawa, K. Arita, Y. Katoh, K. Kawai, S. Muraoka, S. Mitani, S. Fujii, K. Katayama, M. Iijima, T. Mikawa, T. Ninomiya, R. Miyanaga, Y. Kawashima, K. Tsuji, A. Himeno, T. Okada, R.Azuma, K. Shimakawa, H. Sugaya, T. Takagi, R. Yasuhara, K.Horiba, H. Kumigashira, and M. Oshima: Tech. Dig. Internat. Electr. Dev. Meet. (IEDM) (2008) pp. 293.

[25] K. Kinoshita, K. Tsunoda, Y. Sato, H. Noshiro, S. Yagaki, M. Aoki, and Y. Sugiyama: Appl. Phys. Lett. **93**, 033506 (2008).

[26] R. Nakajima, A. Azuma, H. Yoshida, T. Shimizu, T. Ito, and S. Shingubara: Japn. J. Appl. Phys. **57**, 06HD06 (2018).

[27] C. Gopalan, Y. Ma, T. Gallo, J. Wang, E. Runnion, J. Saenz, F. Koushan, P. Blanchard, S. Hollmer: Solid-State Electro. **58**, 54 (2011).

[28] T.-Y. Liu *et al.*: IEEE Internat. Solid-State Circuits Conf. (ISSCC) Dig. Tech. Papers (2013) pp. 210.

[29] M. Arita, A. Tsurumaki-Fukuchi, Y. Takahashi, S. Muraoka, S. Ito, and S. Yoneda: Ext. Abst. Internat. Conf. Solid State Dev. Mater. (SSDM) (2019) pp. 349.

[30] R. Fackenthal, M. Kitagawa, W. Otsuka, K. Prall, D. Mills, K. Tsutsui, J. Javanifard, K. Tedrow, T. Tsushima, Y. Shibahara, and G. Hush: IEEE Internat. Solid-State Circuits Conf.

(ISSCC) Dig. Tech. Papers (2014) pp. 338.

[31] Websites of Business Korea [http://www.businesskorea.co.kr/english/news/ict/13818-chasing-intel-samsung-successfully-develops-3d-cross-point-memory]

[32] M. Miyamura, T. Sakamoto, X. Bai, Y. Tsuji, A. Morioka, R. Nebashi, M. Tada, N. Banno, K. Okamoto, N. Iguchi, H. Hada, T. Sugibayashi, Y. Nagamatsu, S. Ookubo, T. Shirai, F. Sugai, and M. Inaba: IEEE Micro **37**, 32 (2017).

[33] P.-H. Tseng, K.-C. Hsu, Y.-Y. Lin, F.-M. Lee, M.-H. Lee, H.-L. Lung, K.-Y. Hsieh, K. C. Wang, and C.-Y. Lu: Japn. J. Appl. Phys. **57**, 04FE04 (2018).

[34] S. Sills, S. Yasuda, A. Calderoni, C. Cardon, J. Strand, K. Aratani and N. Ramaswamy: Dig. Tech. Sym. VLSI Tech. (2015) pp. T106.

[35] Websites of Nikkei Asian Review [http://asia.nikkei.com/Tech-Science/Tech/Panasonic-UMC-join-to-make-advanced-power-saving-memory]

[36] Ch. Jooss, J. Hoffmann, J. Fladerer, M. Ehrhardt, T. Beetz, L. Wu, and Y. Zhu: Phys. Rev. B **77**, 132409 (2008).

[37] Z. L. Liao, Z. Z. Wang, Y. Meng, Z. Y. Liu, P. Gao, J. L. Gang, H. W. Zhao, X. J. Liang, X. D. Bai, and D. M. Chena: Appl. Phys. Lett. **94**, 253503 (2009).

[38] Z. Xu, Y. Bando, W. Wang, X. Bai, and D. Golberg: ACS Nano **4**, 2515 (2010).

[39] D.-H. Kwon, K. M. Kim, J. H. Jang, J. M. Jeon, M. H. Lee, G. H. Kim, X.-S. Li, G.-S. Park, B. Lee, S. Han, M. Kim, and C. S. Hwang: Nat. Nanotech. **5**, 148 (2010).

[40] T. Fujii, H. Kaji, H. Kondo, K. Hamada, M. Arita, and Y. Takahashi: 2010 IOP Conf. Ser.: Mater. Sci. Eng. **8**, 012033 (2010).

[41] T. Fujii, M. Arita, Y. Takahashi, and I. Fujiwara: Appl. Phys. Lett. **98**, 212104 (2011).

[42] Q. Liu, J. Sun, H. Lv, S. Long, K. Yin, N. Wan, Y. Li, L. Sun, and M. Liu: Adv. Mater. **24**, 1844 (2012).

[43] Y. Yang, P. Gao, S. Gaba, T. Chang, X. Pan, and W. Lu: Nat. Comm. **3**, 732 (2012).

[44] Y. Yang, P. Gao, L. Li, X. Pan, S. Tappertzhofen, S. Choi, R. Waser, I. Valov, and W. D. Lu: Nat. Comm. **5**, 4232 (2014).

[45] F. Pan, S. Gao, C. Chen, C. Song, and F. Zeng: Mater. Sci. Eng. R **83**, 1 (2014).

[46] Y. Takahashi, M. Kudo, and M. Arita: ECS Trans. **69**, 299 (2015).

[47] Y. Yang, Y. Takahashi, A. Tsurumaki-Fukuchi, M. Arita, M. Moors, M. Buckwell, A. Mehonic, and A. J. Kenyon: J. Electroceram. **39**, 73 (2017).

[48] A. Younis, and S. Li: RSC Adv. **8**, 28763 (2018).

[49] M. Arita, A. Tsurumaki-Fukuchi, and Y. Takahashi: Vac. Surf. Sci. **61**, 766 (2018), in Japanese.

[50] W. Sun, B. Gao, M. Chi, Q. Xia, J. J. Yang, H. Qian, and H. Wu: Nat. Comm. **10**, 3453 (2019).

[51] Z. Wang, S. Joshi, S. E. Savel'ev, H. Jiang, R. Midya, P. Lin, M. Hu, N. Ge, J. P. Strachan, Z. Li, Q. Wu, M. Barnell, G.-L. Li, H. L. Xin, R. S. Williams, Q. Xia, and J. J. Yang: Nat. Mater. **16**, 101 (2017).

[52] G.-S. Park, Y. B. Kim, S. Y. Park, X. S. Li, S. Heo, M.-J. Lee, M. Chang, J. H. Kwon, M. Kim, U-I. Chung, R. Dittmann, R. Waser, and K. Kim: Nat. Comm. **4**, 2382 (2013).

[53] J.-Y. Chen, C.-L. Hsin, C.-W. Huang, C.-H. Chiu, Y.-T. Huang, S.-J. Lin, W.-W. Wu, and L.-J. Chen: Nano Lett. **13**, 3671 (2013).

[54] R. J. Kamaladasa, A. A. Sharma, Y.-T. Lai, W. Chen, P. A. Salvador, J. A. Bain, M. Skowronski, and Y. N. Picard: Microsc. Microanal. **21**, 140 (2015).

[55] C.-C. Lin, J.-F. Tang, H.-H. Su, C.-S. Hong, C.-Y. Huang, and S.-Y. Chu: J. Appl. Phys. **119**, 244506 (2016).

[56] Y. Ma, D. Li, A. A. Herzing, D. A. Cullen, B. T. Sneed, K. L. More, N. T. Nuhfer, J. A. Bain, and Marek Skowronski: ACS Appl. Mater. Interfaces **10**, 23187 (2018).

[57] X. Wu, D. Cha, M. Bosman, N. Raghavan, D. B. Migas, V. E. Borisenko, X.-X. Zhang, K. Li, and K.-L. Pey: J. Appl. Phys. **113**, 114503 (2013).

[58] X. Tian, S. Yang, M. Zeng, L. Wang, J. Wei, Z. Xu, W. Wang, and X. Bai: Adv. Mater. **26**, 3649 (2014).

[59] K. Baek, S. Park, J. Park, Y.-M. Kim, H. Hwang, and S. H. Oh: Nanoscale **9**, 582 (2017).

[60] T. Fujii, M. Arita, K. Hamada, H. Kondo, H. Kaji, Y. Takahashi, M. Moniwa, I. Fujiwara, T. Yamaguchi, M. Aoki, Y. Maeno, T. Kobayashi, and M. Yoshimaru: J. Appl. Phys. **109**, 053702 (2011).

[61] M. Kudo, M. Arita, Y. Ohno, T. Fujii, K. Hamada, and Y. Takahashi: Thin Solid Films **533**, 48 (2013).

[62] M. Arita, S. Hirata, A. Takahashi, T. Hiroi, M. Jo, A. Tsurumaki-Fukuchi, and Y. Takahashi: Ext. Abst. Internat. Conf. Solid State Dev. Mater. (SSDM) (2016) pp. 87.

[63] M. Kudo, M. Arita, Y. Takahashi, K. Ohba, M. Shimuta and I. Fujiwara: Proc. IEEE 7th Internat. Memory Workshop (IMW) (2015) pp. 85.

[64] J. Yao, L. Zhong, D. Natelson, and J. M. Tour: Sci. Repts. **2**, 242 (2012).

[65] C.-F. Chang, J.-Y. Chen, C.-W. Huang, C.-H. Chiu, T.-Y. Lin, P.-H. Yeh, and W.-W. Wu: small **13**, 1603116 (2017).

[66] A. Zintler, U. Kunz, Y. Pivak, S. U. Sharath, S. Vogel, E. Hildebrandt, H.-J. Kleebe, L. Alff, and L. Molina-Luna: Ultramicrosc. **181**, 144 (2017).

[67] W. A. Hubbard, A. Kerelsky, G. Jasmin, E. R. White, J. Lodico, M. Mecklenburg, and B. C. Regan: Nano Lett. **15**, 3983 (2015).

[68] M. H. Jang, R. Agarwal, P. Nukala, D. Choi, A. T. C. Johnson, I-W. Chen, and R. Agarwal: Nano Lett. **16**, 2139 (2016).

[69] S. Tappertzhofen, and S. Hofmann: Nanoscale **9**, 17494 (2017).

[70] S. Muto, R. Yonesaka, A. Tsurumaki-Fukuchi, M. Arita, and Y. Takahashi: ECS Trans. **80**, 895 (2017).

[71] T. Fujii, M. Arita, K. Hamada, Y. Takahashi, and N. Sakaguchi: J. Appl. Phys. **113**, 083701 (2013).

[72] H. Kondo, M. Arita, T. Fujii, H. Kaji, M. Moniwa, T. Yamaguchi, I. Fujiwara, M. Yoshimaru, and Y. Takahashi: Japn. J. Appl. Phys. **50**, 081101 (2011).

[73] T. Fujii, M. Arita, Y. Takahashi, and I. Fujiwara: J. Mater. Res. **27**, 886 (2012).

[74] M. Kudo, M. Arita, Y. Ohno, and Y. Takahashi: Appl. Phys. Lett. **105**, 173504 (2014).

[75] M. Arita, Y. Ohno, and Y: Takahashi: Phys. Stat. Sol. A **213**, 306 (2016).

[76] M. Arita, Y. Ohno, Y. Murakami, K. Takamizawa, A. Tsurumaki-Fukuchi, and Y. Takahashi: Nanoscale **8**, 14754 (2016).

[77] M. Arita, A. Takahashi, Y. Ohno, A. Nakane, A. Tsurumaki-Fukuchi, and Y. Takahashi: Sci.

Repts. **5**, 17103 (2015).

[78]  Y. Y. Chen, B. Govoreanu, L. Goux, R. Degraeve, A. Fantini, G. S. Kar, D. J. Wouters, G. Groeseneken, J. A. Kittl, M. Jurczak, and L. Altimime: IEEE Trans. Electr. Dev. **59**, 3243 (2012).

[79]  J. Yoon, J. Lee, H. Choi, J.-B. Park, D. Seong, W. Lee, C. Cho, S. Kim, and H. Hwang: Microel. Eng. **86**, 1929 (2009).

[80]  D. Kumar, R. Aluguri, U. Chand, and T.-Y. Tseng: Appl. Phys. Lett. **110**, 203102 (2017).

[81]  S. K. Vishwanath, H. Woo, and S. Jeon: Nanotech. **29**, 235202 (2018).

[82]  J. H. Shin, Q. Wang, and W. D. Lu: IEEE Electr. Dev. Lett. **39**, 1512 (2018).

[83]  K.-J. Gan, P.-T. Liu, Y.-C. Chiu, D.-B. Ruan, T.-C. Chienb, and S. M. Sze: Surf. Coat. Technol. **354**, 169 (2018).

[84]  M. Arita, R. Ishikawa, S. Hirata, A. Tsurumaki-Fukuchi, and Y. Takahashi: Ext. Abst. Internat. Conf. Solid State Dev. Mater. (SSDM) (2017) pp. 39.

[85]  R. Ishikawa, S. Hirata, A. Tsurumaki-Fukuchi, M. Arita, Y. Takahashi, M. Kudo, and S. Matsumura: ECS Trans. **80**, 903 (2017).

[86]  M. Arita, R. Ishikawa, A. Tsurumaki-Fukuchi, and Y. Takahashi: Ext. Abst. Internat. Conf. Solid State Dev. Mater. (SSDM) (2019) pp. 703.